Study of the $I \cdot CO_2$ van der Waals Complex by Threshold Photodetachment Spectroscopy of I^-CO_2

Yuexing Zhao,† Caroline C. Arnold and Daniel M. Neumark*‡
Department of Chemistry, University of California, Berkeley, CA 94720, USA and Chemical Sciences Division, Lawrence Berkeley Laboratory, Berkeley, CA 94729, USA

Photodetachment of the I^-CO_2 anion accesses the three lowest-lying electronic states of the $I \cdot CO_2$ van der Waals complex. High-resolution threshold photodetachment (ZEKE) spectroscopy reveals progressions in the low-frequency C—I van der Waals stretch in each electronic state, providing a detailed spectroscopic probe of the interaction between a halogen atom and a closed-shell molecule. From our data, we construct one-dimensional potential-energy functions for each neutral state as well as for the anion, and these are compared to rare-gas–halogen and rare-gas–halide potentials.

The development of intermolecular potentials between weakly interacting species has received much attention in recent years. A host of spectroscopic and scattering-based experiments have been performed to probe these fundamental interactions. While the most commonly studied examples are the interactions between closed-shell atoms and molecules, the more complex potentials between open-shell and closed-shell species are also of considerable interest. The simplest examples of these are rare-gas halides (Rg–X), which have been studied extensively because of their importance in excimer lasers. More complicated systems include the van der Waals complexes between rare-gas atoms and molecular radicals, such as ArOH [1–3] and ArNO.[4] In this paper we present results for the $I \cdot CO_2$ complex, which we study by high-resolution photodetachment spectroscopy of the I^-CO_2 anion. Since the $I \cdot CO_2$ and Rg–X interactions have much in common, our experiment is best understood in the context of the somewhat simpler Rg–X systems.

In contrast to the isotropic interaction between two closed-shell atoms, the potential between a rare gas and halogen atom is complicated by spin–orbit and orientation effects due to the open-shell nature of the halogen atom.[5,6] These effects lead to the three electronic states shown in the correlation diagram, Fig. 1. At infinite Rg–X separations, we have the two $^2P_{3/2}$ and $^2P_{1/2}$ spin–orbit levels of the halogen atom. As the separation decreases, the electrostatic interactions between the two atoms becomes increasingly important, resulting in a splitting of the $^2P_{3/2}$ level. The overall interaction is best described by Hund's case (c) coupling at large distances, where the spin–orbit interaction dominates, and by Hund's case (a) coupling at small distances, where electrostatic effects are dominant. Typically, all three curves have shallow minima, and the determination of the well depths and locations is one of the prime targets of any investigation of Rg–X species. Haberland[5] and Aquilanti *et al.*[6] have shown that, if the spin–orbit interaction is independent of distance, then the potential-energy curves associated with the three electronic states are not independent; from two of the curves, the third may be calculated.

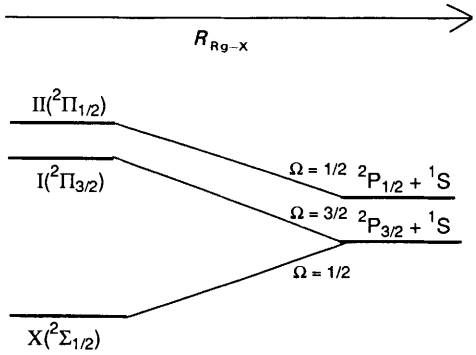

Fig. 1 Schematic correlation diagram showing the three electronic states arising from rare gas (Rg) + halogen (X) interaction. In order of increasing energy, these are called the X $\frac{1}{2}$, I $\frac{3}{2}$ and II $\frac{1}{2}$ states.

† University Fellow, University of California.
‡ NSF Presidential Young Investigator and Dreyfus Teacher-Scholar.

Previous experimental work on Rg–X systems includes both scattering experiments and spectroscopic studies. Lee and co-workers[7] have extracted Rg–X potential-energy curves in a series of differential cross-section measurements, while Aquilanti *et al.*[8] have measured integral cross-sections for several Rg–X pairs as a function of collision energy to obtain this information. As for spectroscopic studies, except for an absorption experiment by Smith and Kobrinsky,[9] all the gas-phase experiments on Rg–X complexes have been implemented by using emission spectroscopy. Spontaneous emission spectra have been recorded by Ewing and Brau,[10] Golde and Thrush,[11] Tellinghuisen and co-workers[12] and Casassa *et al.*[13] With the exception of several band systems in XeF and XeCl,[10,12] all of the observed spectra show only the diffuse structure characteristic of bound–free transitions. More structure has been observed in the emission[14–16] and predissociation[17] spectra of the series of heteronuclear cations $HeNe^+$, $NeAr^+$ *etc.* Each of these is isoelectronic with an Rg–X pair and has the same qualitative electronic structure, although the ground states of the ions are far more strongly bound than the corresponding Rg–X species. Rare-gas diatomic cations have also been studied by photoionization and photoelectron spectroscopy[18–20] of the corresponding neutral van der Waals molecule.

The approach used in our laboratory to study the $I \cdot CO_2$ complex is most akin to the last approach.[19,20] We perform high-resolution threshold photodetachment (ZEKE) spectroscopy on I^-CO_2. This work is a continuation of our lower-resolution photoelectron spectroscopy studies of $I^-(CO_2)_n$ clusters.[21] Photodetachment of I^-CO_2 accesses three neutral electronic states analogous to those shown in Fig. 1, and the resolution of the spectra reported here is sufficient to resolve vibrational progressions due to the I–CO_2 van der Waals stretch for each electronic state. From these data we construct one-dimensional potential-energy curves for the anion

and the three neutral states. The photoelectron spectrum showed that the I^-CO_2 anion is bound by *ca.* 0.2 eV, and the neutral states are expected to be bound by considerably less. Hence, the situation is reversed from the rare-gas diatom photoelectron spectra mentioned above, in which the cation resulting from photoionization is more strongly bound than the neutral van der Waals molecule.

Experimental

The high-resolution threshold photodetachment spectrometer (also called a zero electron kinetic energy or ZEKE spectrometer) has been described in detail previously.[22] Briefly, an internally cold I^-CO_2 beam is generated by expanding a 2–4% mixture of HI in CO_2 gas (or a mixture of CO_2 and He gas) through a pulsed molecular beam valve, typically with a backing pressure of 60 psi,† and then crossing the molecular beam with a 1 keV electron beam just outside the valve orifice. Negative ions are formed through dissociative attachment and clustering processes in the continuum flow region of the free-jet expansion and their internal degrees of freedom are cooled as expansion progresses. We achieved a vibrational temperature of *ca.* 65 K in this case. The negative ions that pass through a 2 mm diameter skimmer are collinearly accelerated to 1 keV and mass-selected with a 1 m long beam-modulated time-of-flight mass spectrometer.[23] The mass selected ions then enter the detection region where they are photodetached by an excimer-pumped dye laser. QUI and rhodamine 590 laser dyes were used and the latter was doubled with a BBO crystal.

Only those electrons produced with nearly zero kinetic energy are detected by using a detection scheme based on the design of Muller-Dethlefs *et al.*[24] for ZEKE photoionization of neutral species. First, a delay of 150–200 ns subsequent to photodetachment allows the more energetic electrons and the threshold electrons to separate. A weak field (*ca.* 5 V cm^{-1}) is then applied collinearly to extract the photoelectrons. Finally ZEKE electrons are selectively detected by using a combination of spatial and temporal filtering. The ultimate resolution of the instrument is 0.3 meV. However, under the operating conditions used in these experiments the resolution was *ca.* 1.0 meV. The electron signal is normalized to laser power and ion signal.

Results

Spectrum and General Features

The threshold photodetachment spectrum of I^-CO_2 is shown in Fig. 2. The lower resolution (*ca.* 80 cm^{-1}, dotted lines) photoelectron spectrum of Arnold *et al.*[21] is superimposed for comparison. Both spectra consist of two distinct bands separated approximately by the $I(^2P)$ spin–orbit splitting (0.943 eV). We refer to these two bands as the $I(^2P_{3/2})\cdot CO_2$ band [Fig. 2(*a*)] and, at higher energy, the $I(^2P_{1/2})\cdot CO_2$ band [Fig. 2(*b*)]. In the photoelectron spectrum, both bands consisted of a short progression of peaks spaced by 670 ± 50 cm^{-1}. This spacing is equal to the CO_2 bend frequency (667 cm^{-1}), and these peaks were assigned to progressions in the CO_2 bend in the neutral complex (the ν_2 mode) which arise because the CO_2 is slightly bent in the anion (175°) but linear in the neutral. The anion is expected to have a C_{2v} structure with the I^- bound to the C atom, and we attributed the bent CO_2 moiety to a small amount of charge transfer from the I^- to the CO_2 LUMO.[21]

† 1 psi = 6.894 76 × 10^3 Pa.

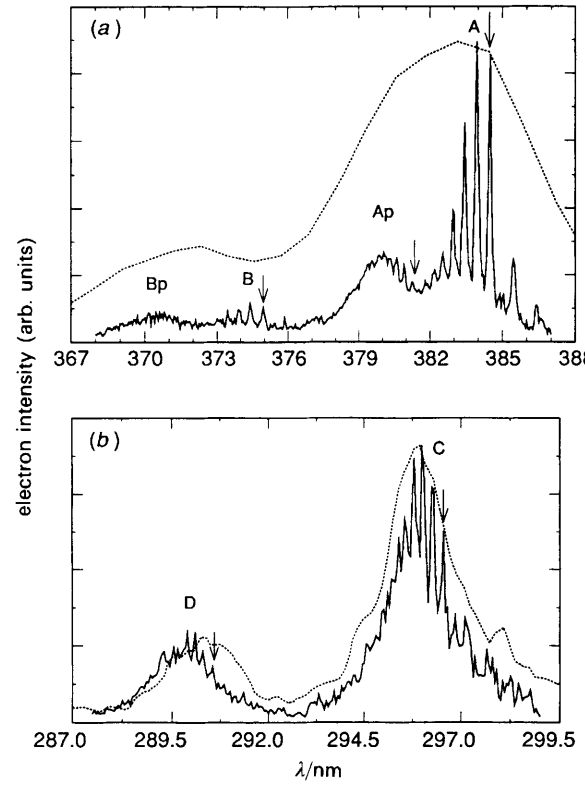

Fig. 2 Threshold photodetachment spectrum of I^-CO_2 (solid lines) and photoelectron spectrum (from ref. 21) of I^-CO_2 (dotted lines). (*a*) $I(^2P_{3/2})\cdot CO_2$ band and (*b*) $I(^2P_{1/2})\cdot CO_2$ band. The arrows indicate the band origins.

The threshold photodetachment spectra show considerably more structure. The $I(^2P_{3/2})\cdot CO_2$ band now consists of four sub-bands, labelled A, Ap, B, and Bp in Fig. 2(*a*). Bands Ap and B lie to the blue of band A by 225 and 662 cm^{-1} (approximately the CO_2 bend frequency), respectively, and band Bp lies *ca.* 225 cm^{-1} to the blue of band B. Each of these bands shows additional low-frequency structure. In band A, we observe a progression with spacings starting at 37 cm^{-1} and gradually decreasing to the blue; the origin of this progression is indicated by an arrow. The peaks are 9–12 cm^{-1} wide (FWHM). We also observe two smaller peaks in band A to the red of the origin which are separated by 64 cm^{-1}. These appear to be anion hot bands, since their intensities vary with source conditions. The low-frequency structure in band A is essentially mirrored in band B, although the intensity is considerably less. In band Ap, the peak spacings are smaller than in band A, and a continuum appears at the high-energy side of the band. Again, the overall appearance of band Bp is similar but the intensity is less. In the $I(^2P_{1/2})\cdot CO_2$ band [Fig. 2(*b*)], we observe only two sub-bands labelled C and D. The band origins are separated by 697 cm^{-1}, and each band consists of a progression of peaks whose spacing decreases from *ca.* 30 cm^{-1} towards the blue, eventually resulting in an apparent continuum.

Spectrum Assignments

The overall features in the I^-CO_2 ZEKE spectrum can be readily explained in terms of the electronic and vibrational structure of the $I\cdot CO_2$ complex. We first consider the significance of the spacings near 670 cm^{-1} observed between several pairs of sub-bands. Based on our interpretation of the photoelectron spectrum,[21] this is the frequency of the $\nu_2(CO_2)$ bending mode in the $I\cdot CO_2$ complex. From the comparison of the ZEKE spectrum to the photoelectron

spectrum, we assign sub-bands A and Ap in the $I(^2P_{3/2})\cdot CO_2$ band and sub-band C in the $I(^2P_{1/2})\cdot CO_2$ band to transitions to the $v_2 = 0$ bending level of the neutral complex, and sub-bands B, Bp and C to transitions to the $v_2 = 1$ level.

This assignment requires an explanation of why there are two sub-bands corresponding to each v_2 level in the $I(^2P_{3/2})\cdot CO_2$ band but not in the $I(^2P_{1/2})\cdot CO_2$ band. This is an electronic effect which can be explained with reference to the correlation diagram in Fig. 1. Specifically, at sufficiently small distance, the electrostatic interaction between the I atom and CO_2 molecule should split the $I(^2P_{3/2})$ atomic level into two levels with $\Omega = 1/2$ and $\Omega = 3/2$, (the X $\frac{1}{2}$ and I $\frac{3}{2}$ states) whereas the $I(^2P_{1/2})$ level is not split by this interaction, leaving only a single $\Omega = 1/2$ level (the II $\frac{1}{2}$ state). Here Ω is the projection of the total electronic angular momentum on the C–I axis. Strictly speaking, it is defined only for a diatomic molecule, but it should be an approximately good quantum number considering the relatively weak interaction between the I atom and CO_2 molecule.

In any case, we interpret the threshold photodetachment spectrum to mean that the 225 cm^{-1} interval between bands A and Ap and bands B and Bp is the splitting between the X $\frac{1}{2}$ and I $\frac{3}{2}$ levels of the $I\cdot CO_2$ complex. This assignment is supported by the absence of a comparable splitting in the $I(^2P_{1/2})\cdot CO_2$ band. We therefore assign bands A, Ap and C to transitions to the X $\frac{1}{2}$, I $\frac{3}{2}$ and II $\frac{1}{2}$ levels of the $I\cdot CO_2$ complex with $v_2 = 0$, and bands B, Bp and D to the analogous transitions with $v_2 = 1$. Note that we are clearly in the Hund's case (c) regime; the electrostatically induced splitting is not only less than the I atom spin–orbit splitting, it is also less than the CO_2 bend frequency. Fig. 3 shows the anion and neutral potential-energy curves responsible for the bands in the ZEKE spectrum. These curves are discussed in more detail below.

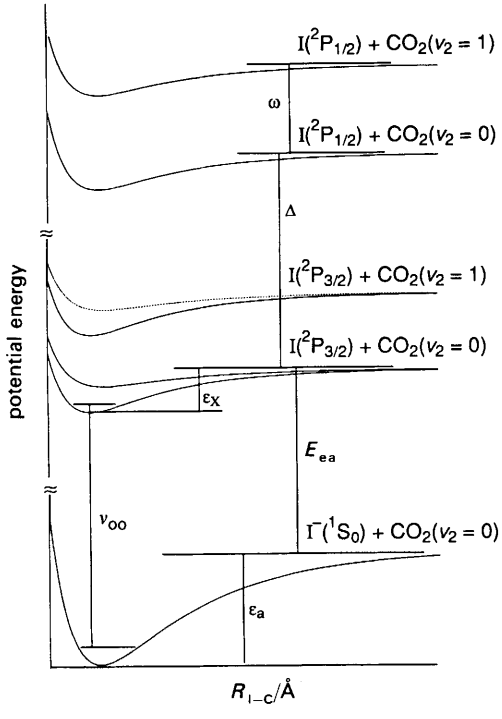

Fig. 3 Illustration of the potential-energy curves responsible for the bands in Fig. 2. The bottom potential-energy curve corresponds to the anion state, while the remaining curves, in order of increasing energy, correspond to the following neutral states: X $\frac{1}{2}$ (band A), I $\frac{3}{2}$ (band Ap), X $\frac{1}{2}$ (band B, $v_2 = 1$), I $\frac{3}{2}$ (band Bp, $v_2 = 1$), II $\frac{1}{2}$ (band C) and II $\frac{1}{2}$ (band D, $v_2 = 1$). ε_x and ε_a are the well depths for the neutral X $\frac{1}{2}$ state and the anion state, respectively; v_{00} is the origin transition energy for band A; E_{ea} is the electron affinity of I; Δ is the $I(^2P)$ spin–orbit splitting constant and ω the bending frequency of CO_2.

We next consider the low-frequency vibrational progressions seen in each of the sub-bands. With peak spacings in the range of 30 cm^{-1}, these must be progressions in one of the van der Waals modes of the $I\cdot CO_2$ complex. Extended progressions in photodetachment spectroscopy generally involve totally symmetric vibrational modes. If the neutral complex is T-shaped with the I atom weakly bound to the C atom, then the only totally symmetric van der Waals mode is the C—I stretch (the v_3 mode). This is a reasonable assignment, since photodetachment should affect the C—I bond length and one therefore expects extensive progressions in this mode. This assignment implies that the hot bands in band A represent a progression in the C—I stretch of the anion. The higher frequency, 64 cm^{-1}, is consistent with the stronger binding expected in the anion. Other possible $I\cdot CO_2$ geometries are discussed in the last section of this paper.

The van der Waals progressions in the sub-bands corresponding to the various electronic states of the neutral are quite different. Band A (X $\frac{1}{2}$ state) shows the most pronounced structure, while in band Ap (I $\frac{3}{2}$ state), the progression is shorter, the peak spacing is smaller, and there appears to be a continuum towards the blue. The progression in band C (II $\frac{1}{2}$ state) is intermediate in length and peak spacing. This suggests that the well depths for the three electronic states decrease in the order X $\frac{1}{2}$ > II $\frac{1}{2}$ > I $\frac{3}{2}$, a result predicted in the previous work on Rg–X potentials. The other notable result is that the appearance of the van der Waals progression is largely independent of v_2, the bending quantum in the neutral vibration. For example, apart from overall intensities, bands A and B are quite similar (although not identical) in appearance. This means the vibrational wavefunction for the two modes can be written as

$$\Psi_{v_2^{\prime\prime}, v_3}(Q_2, Q_3) \cong \Psi_{v2}(Q_2)\Psi_{v3}(Q_3) \quad (1)$$

where $\Psi_{v_2}(Q_2)$ may depend weakly on v_3 and *vice versa*.

The positions and assignments of peaks in each band are tabulated in Tables 1 and 2. Band Bp is not listed due to its low intensity; individual peaks could not be picked out readily.

Analysis

Based on the qualitative assignments discussed in the previous section, we can construct potential-energy curves for I^-CO_2 and the three electronic states of $I\cdot CO_2$ from which the experimental spectra can be simulated. This section describes the simulation method and the form of the resulting potential-energy curves. We restrict ourselves to a determination of the one-dimensional potential-energy curves along the C—I (v_3) van der Waals stretch coordinate that reproduce the individual sub-bands in Fig. 2(*a*) and (*b*). This approach is reasonable in light of eqn. (1) above, although it neglects any coupling of the C—I stretch to the low-frequency van der Waals bending modes.

Method of Calculation

For a given set of model potentials for the anion and neutral, we simulate the spectrum by (*a*) solving for the eigenvalues and eigenfunctions supported on each potential and (*b*) calculating the Franck–Condon overlap between the first few anion v_3 levels and the bound and continuum levels supported by the neutral potential-energy curves. We use a discrete variable representation (DVR) to determine the eigenvalues and eigenfunctions.[25–27] Our implementation of the DVR to the problem at hand has been described else-

Table 1 Peak positions, relative energies and assignments for Fig. 2(*a*) [$I(^2P_{3/2})\cdot CO_2$ band]

band	position /nm	vacuum wavenumber /cm^{-1}	relative energy /cm^{-1}	assignment
A	386.25	25882	−129	3_2^0
	385.30	25946	−65	3_1^0
	384.35	26011	0	origin[a] $(2_0^0 3_0^0)$
	383.80	26048	37	3_0^1
	383.30	26082	71	3_0^2
	382.85	26113	102	3_0^3
	382.40	26143	132	3_0^4
	382.03	26169	158	3_0^5
	381.68	26193	182	3_0^6
Ap	381.05	26236	0	origin $(2_0^0 3_0^0)$
	380.75	26257	21	3_0^1
	380.45	26278	42	3_0^2
	380.17	26297	61	3_0^3
	379.91	26315	79	3_0^4
	379.70	26329	93	3_0^5
B	375.71	26608	−65	3_1^0
	374.80	26673	0	origin $(2_0^1 3_0^0)$
	374.26	26711	38	3_0^1
	373.77	26746	73	3_0^2
	373.31	26779	106	3_0^3

[a] This corresponds to an electron affinity of 3.225 (0.001) eV.

where.[28] We use a standard version in which the DVR points are determined by diagonalization of the position operator in a one-dimensional harmonic oscillator basis (Gauss–Hermite quadrature). Even for our relatively simple problem, the DVR offers a great increase in speed as we do not have to set up and diagonalize a new Hamiltonian matrix for each model potential.

The one somewhat non-standard aspect of our calculation is that we need to treat continuum as well as bound-state wavefunctions. To simulate the continuum transitions, we use the approach outlined in ref. 28. When we use the DVR procedure to determine eigenvalues supported by a potential with a shallow well, we obtain a discrete energy spectrum

Table 2 Peak positions, relative energies and assignments for Fig. 2(*b*) [$I(^2P_{1/2})\cdot CO_2$ band]

band	position /nm	vacuum wavenumber /cm^{-1}	relative energy − cm^{-1}	assignment
C	297.65	33586	−125	3_2^0
	297.10	33648	−63	3_1^0
	296.84	33678	−33	3_1^1
	296.55	33711	0	origin $(2_0^0 3_0^0)$
	296.26	33744	33	3_0^1
	295.99	33775	64	3_0^2
	295.77	33800	89	3_0^3
	295.54	33826	115	3_0^4
	295.39	33844	133	3_0^5
D	290.54	34408	0	origin $(2_0^1 3_0^0)$
	290.29	34438	30	3_0^1
	290.08	34463	55	3_0^2
	289.88	34486	78	3_0^3

both above and below the dissociation continuum; the discrete levels above the dissociation limit are an artifact resulting from using localized (*i.e.* harmonic oscillator) basis functions. If the number of basis functions is changed, the continuum 'eigenvalues' change substantially, while the bound eigenvalues are relatively unaffected. Therefore, by doing the DVR and Frank–Condon calculations at several different basis sizes, summing the results together, and convoluting the resulting stick spectra with our experimental resolution, we generated a simulated spectrum which is discrete below the dissociation continuum and continuous above it. The full simulation requires summing between eight and twelve simulations in our case. The accuracy of this method was checked by comparing the full simulation to the results of a one-dimensional time-dependent wavepacket calculation[29] using the same potential-energy curves; the two methods yield identical results.

Nature of the Potential-energy Curves

It is desirable to use the simplest potential-energy functions needed to fit our spectra. The long-range attractive forces are well understood for the neutral and anion. For the various $I\cdot CO_2$ states, the leading term in the potential at long range is the $-1/r^6$ term due to the van der Waals attraction, while for I^-CO_2, the long-range attraction goes as $-1/r^4$ due to charge–quadrupole and charge–induced dipole interactions with a contribution from a $-1/r^6$ term due to the large polarizability of I^-. There is considerably less agreement on the form of the potential at closer range, and, for example, one can choose for the neutral functional forms ranging from the Lennard-Jones (12-6) potential to the considerably more involved functions developed by Lee,[7] Aquilanti[8] and their co-workers.

We experimented with several anion and neutral potential-energy functions to see which gave the best results for band A, since it is the most structured and intense band in the spectrum and includes the most distinct anion hot bands. The following procedure was used. Given a functional form for the neutral potential (the $X\,\frac{1}{2}$ state), the parameters were varied so that the bound states energies agreed with the experimental peak spacings (band A has no observable continuum transitions). The parameters in the anion potential were then adjusted to match the absolute peak positions, the hot-band transition energies, and the intensity distribution of all the peaks.

Although we were able to reproduce the peak spacings in band A fairly well using the Lennard-Jones (12-6) potential for the neutral, the best simulation of peak positions and intensities was obtained with the Maitland–Smith (*n*-6) potential[30] for the neutral:

$$U(r^*) = \frac{\varepsilon}{n-6}\left[6(r^*)^{-n} - n(r^*)^{-6}\right] \qquad (2)$$

Here $r^* = r/r_m$, where r_m is the distance at the potential minimum energy ε. The key feature of this potential is that n varies with r^* according to

$$n = m + \gamma(r^* - 1) \qquad (3)$$

where m and γ are adjustable parameters. The Maitland–Smith type potential is a simple potential form but is flexible enough to fit our data. The exponent of the repulsive part varies with distance depending on the sign of γ, while the attractive part is still represented by the $-1/r^6$ term. Notice the Lennard-Jones (12-6) form is obtained when m is set to 12 and γ is set to zero. Using eqn. (2) we obtain the best match with experiment for $\varepsilon = 44.5$ meV, $r_m = 3.99$ Å, $m = 11.8$ and $\gamma = -2.5$ for the neutral $X\,\frac{1}{2}$ state.

Once the well depth ε_X of the X $\frac{1}{2}$ state has been determined, we can immediately extract the well depth ε_a of the anion potential from the following formula:

$$\nu_{00} + \omega_0^a + \varepsilon_X - \omega_0^X = \varepsilon_a + E_{ea}(I) \quad (4)$$

Here $\nu_{00} = 3.225$ eV is the energy of the origin transition for band A, $E_{ea}(I) = 3.0591$ eV is the electron affinity of atomic iodine, and ω_0^a and ω_0^X are the zero-point energies of the anion state and the neutral X $\frac{1}{2}$ state, respectively. Eqn. (4) is evident from Fig. 3. From our X $\frac{1}{2}$ state potential we find $\omega_0^X = 20$ cm^{-1}, and we estimate $\omega_0^a = 32$ cm^{-1} from the hot-band spacings in band A. From this we obtain $\varepsilon_a = 212$ meV.

To construct the full anion potential, we use a variation of eqn. (2):

$$U(r^*) = \frac{\varepsilon_a}{n-4}\left[4(r^*)^{-n} - n(r^*)^{-4}\right] \quad (5)$$

which we refer to as the Maitland–Smith (n-4) potential. Compared to the neutral potential, the attractive part for the anion is represented by the $-1/r^4$ term. The best simulation of band A is obtained with $r_m = 3.772$ Å, $m = 10$ and $\gamma = 1.5$. Note that r_m for the anion is smaller than for the neutral $X_{1/2}$ state. Simulations with r_m larger in the anion than the neutral yielded insufficient intensities in the high ν_3 peaks. Given the anion potential and the neutral X $\frac{1}{2}$ potential established from simulation of band A, the hot-band transition intensities in band A are best reproduced by using 65 K as the anion vibrational temperature.

Once the anion well depth is determined, we can use energy-balance equations similar to eqn. (4) to find the well depths for the potential-energy curves responsible for bands Ap, B, C and D, using the experimentally measured band origins. (Fig. 3 is again a useful reference.) The zero-point energies needed to extract the well depths can be estimated from the peak spacings in each band. The well depths obtained by this method are listed in Table 3.

Finally, using the anion potential obtained above, we can construct the full potential-energy curves for the excited states responsible for bands Ap, B, C and D. We found we could simulate bands C and D with a simple Lennard-Jones (12-6) potential, but the Maitland–Smith (n-6) form was required to simulate bands Ap and B. The potential parameters for the excited states are tabulated in Table 3. Note that the well depth for the band C potential is 4.5 meV deeper than for the band D potential. This indicates that the attraction between $I(^2P_{1/2})$ and CO_2 is slightly reduced for bend-excited CO_2, effectively increasing the CO_2 bend frequency in the $I(^2P_{1/2})\cdot CO_2$ complex.

Fig. 4 shows the simulated and experimental spectra. Because we ignored the CO_2 bending mode in our simulation, the simulated bands are simply scaled by multiplying the peak intensities in each band by a constant so that we can compare the simulated data to the experimental results. The four potentials for the neutral states X $\frac{1}{2}$, I $\frac{3}{2}$ and II $\frac{1}{2}$ with $\nu_2 = 0$ (corresponding to band A, AP and C) and the anion state are drawn in Fig. 5.

Table 3 Potential parameters for the anion and the neutral states obtained from the simulation (the potential forms are those discussed in the text)

state (band)	ε/meV	r_m/Å	m	γ
X $\frac{1}{2}$ (A)	44.5	3.990	11.8	−2.5
X $\frac{1}{2}$ (B)	44.5	3.995	11.8	−2.5
I $\frac{3}{2}$ (Ap)	17.0	4.147	14.0	9.5
II $\frac{1}{2}$ (C)	32.0	4.083	12.0	0
II $\frac{1}{2}$ (D)	27.5	4.090	12.0	0
anion	212.0	3.773	9.0	1.5

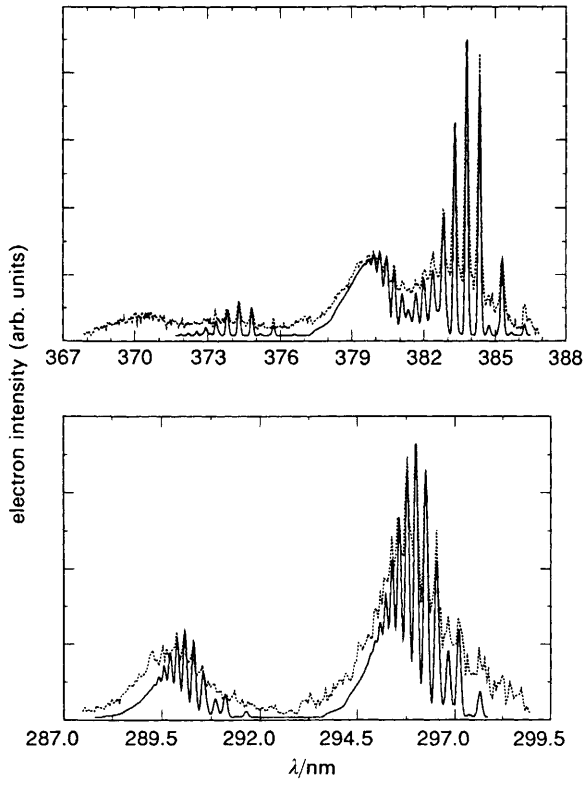

Fig. 4 Frank–Condon simulation of the threshold photodetachment spectrum of I^-CO_2. The solid lines are the simulated results, the dotted lines are the experimental results.

It is important to consider the possible errors in the potential-energy functions and parameters, in particular, the values for ε and r_m. We can estimate the uncertainties in these two parameters by systematically varying them and observing when the agreement between the simulated and experimental spectra degrades. The estimated maximum uncertainties are ±8% in ε for the neutral states and r_m for

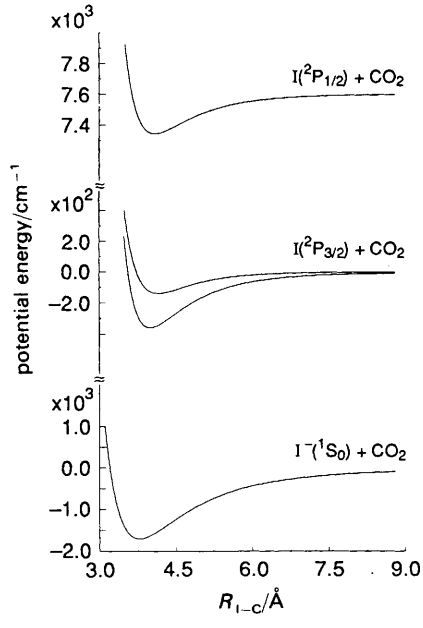

Fig. 5 Anion and three neutral adiabatic potential-energy curves resulting from our fit to the $\nu_2 = 0$ bands in the spectrum. Note that the Y-axis scale for the anion potential is larger than that for the neutral potentials.

all the states and ±2% in ε for the negative ion state. As for the full potential-energy functions, our spectra probe the attractive wells and (for bands Ap, C and D) the repulsive wall a few hundred cm^{-1} above the dissociation limit. We believe that these regions of the curves are well characterized. However, our experiment is clearly not sensitive to the repulsive wall at higher energies, and the characterization of this region of the potential will have to await scattering measurements of the differential and total cross-sections.

Another independent check on our well depths can be obtained by applying the method of LeRoy and Bernstein,[31] who showed that the dissociation energy can be obtained given the long-range attractive potential and the energies of several vibrational levels near the dissociation limit. This analysis has recently been used by Lessen and Brucat[32] to obtain dissociation energies for rare-gas–transition-metal cations. If we apply this to the neutral states, using a $-1/r^6$ attractive potential, we obtain $\varepsilon = 36$ meV for band A, 19 meV for band Ap and 34 meV for band C. The results for band Ap and C are fairly close (*ca.* 2 meV) to the values in Table 3, while the result for band A differs, the well depth for band A is off by 10 meV. The greater deviation for band A is not surprising, since we actually do not observe vibrational levels up to the dissociation limit as we do for the other two bands.

Discussion

In this section, we examine in more detail some features of the I^-CO_2 and $I \cdot CO_2$ potential-energy curves obtained in the previous section. The first point to consider is the change in the C—I bond length upon photodetachment. For weakly bound molecules or ions, the length of the weak bond is determined by the strength of the attractive interaction and the sizes of the atoms most involved in the bond. In our case, these two factors compete: the anion is more strongly bound than the neutral, but I^- is larger than I in the sense that the polarizability of I^- is larger. Our analysis does in fact show that the C—I bond length in the anion is 0.22 Å smaller than the neutral X $\frac{1}{2}$ state, the most strongly bound neutral state. This result is consistent with previous work on Rg–X systems.[6–8,33] With the exception of XeF and XeCl,[10,12] the bond lengths are shorter in the anion than in the neutral.

One question raised by our analysis is the validity of the one-dimensional approach, in which we essentially treat the CO_2 molecule as if it were an atom. One check on this is provided by the work of Haberland[5] and Aquilanti *et al.*[6] on Rg–X systems. They showed that given two of the three adiabatic Rg–X potentials, the third can be calculated if one assumes the spin–orbit constant is independent of the internuclear distance. [See eqn. (8) below.] If we use their expressions, and calculate the I $\frac{3}{2}$ potential from our X $\frac{1}{2}$ and II $\frac{1}{2}$ curves, we find $\varepsilon = 23$ meV and $r_m = 4.19$ Å. These are close but not identical to the results in Table 3 ($\varepsilon = 17.3$ meV and $r_m = 4.15$ Å). Some of this discrepancy may occur because the spin–orbit coupling is not a constant, and some may occur because CO_2 is not an atom. Nonetheless, the values for r_m and ε are sufficiently close that we believe our one-dimensional analysis is appropriate. This means that we can further analyse our potentials in terms of the formalism developed for Rg–X species.

In the absence of spin–orbit coupling, the interaction potential between a rare gas and halogen atom can be written as[6]

$$V(r, \theta) = V_0(r) + V_2(r)P_2(\cos\theta) \qquad (6)$$

where r is the internuclear distance and θ is the angle between the unfilled p orbital on the halogen atom and the internuclear axis. Thus, $V_2(r)$ represents the anisotropic interaction between two atoms due to an unfilled orbital on one of the atoms. $V_0(r)$ and $V_2(r)$ are related to the potentials $V_\Sigma(r)$ and $V_\Pi(r)$ that describe the Σ and Π states resulting from the Rg + X interaction without spin–orbit coupling by

$$V_0 = \tfrac{1}{3}(V_\Sigma + 2V_\Pi); \qquad V_2 = \tfrac{5}{3}(V_\Sigma - V_\Pi) \qquad (7)$$

Once either V_Σ and V_Π or V_0 and V_2 are specified, along with the spin–orbit coupling constant Δ, one can find the three potentials $V(X\ \frac{1}{2})$, $V(I\ \frac{3}{2})$, $V(II\ \frac{1}{2})$:[5,6]

$$V(X\ \tfrac{1}{2}) = V_0 + \frac{V_2}{10} + \frac{\Delta}{2} - \frac{1}{2}\left(\frac{9}{25}V_2^2 + \Delta^2 - \frac{2}{5}V_2\Delta\right)^{1/2}$$

$$V(I\ \tfrac{3}{2}) = V_0 - \frac{V_2}{5}$$

$$V(II\ \tfrac{1}{2}) = V_0 + \frac{V_2}{10} + \frac{\Delta}{2} + \frac{1}{2}\left(\frac{9}{25}V_2^2 + \Delta^2 - \frac{2}{5}V_2\Delta\right)^{1/2} \qquad (8)$$

Conversely, given two of the three potentials $V(X\ \frac{1}{2})$, $V(I\ \frac{3}{2})$, $V(II\ \frac{1}{2})$, one can determine V_Σ, V_Π, V_0 and V_2.

If we do this using our $V(X\ \frac{1}{2})$ and $V(II\ \frac{1}{2})$ potentials for $I \cdot CO_2$ (with $v_2 = 0$), we obtain the curves for V_Σ, V_Π, V_0 and V_2 shown in Fig. 6. We find that for $V_0(r)$, $\varepsilon = 32$ meV and $r_m = 4.08$ Å, while $V_2(r)$ is purely attractive. This means that as the I and CO_2 approach, the unfilled p orbital prefers to lie along the C–I axis. A similar tendency also can be seen by comparing the $V_\Sigma(r)$ and $V_\Pi(r)$ curves: the well is noticeably deeper for the Σ state. These anisotropic effects strongly resemble those in Rg–X potentials.[7,8] Fig. 6 shows that $|V_2/\Delta|$ is small (≤ 0.15) over the range of R_{C-I} probed in our experiment, indicating, as expected, that we are in the Hund's case (c) coupling regime; the transition from case (c) to case (a) occurs in the neighbourhood of $|V_2/\Delta| = 1$.

In Table 4 we compare our well depths and r_m values for $I \cdot CO_2$ with those for similar Rg–X species. The polarizability of CO_2 is less than that of Xe and about equal to that of Kr,[34] and this is consistent with the r_m values: $r_m(XeI) > r_m(KrI) \approx r_m(I \cdot CO_2)$. However, the $I \cdot CO_2$ well for the ground X $\frac{1}{2}$ state is noticeably deeper than for XeI and KrI. The greater well depth is most likely due to the interaction of the CO_2 quadrupole moment with the I atom polarizability. This interaction apparently has a larger effect on the well depth than on r_m. Although the binding energies of XeI^- and KrI^- have not been experimentally determined, Capelletti *et*

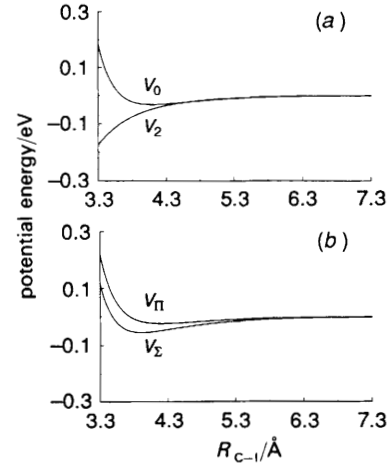

Fig. 6 Plot of the potentials $V_0(r)$, $V_2(r)$, $V_\Sigma(r)$ and $V_\Pi(r)$ obtained from the potentials in Fig. 5. See eqn. (6)–(8) in the text.

Table 4 Comparisons of our well depth ε and r_m values for $I \cdot CO_2$ with those for a few similar Rg–X species

		$V(X\ ^1/_2)$		$V(I\ ^3/_2)$		$V(II\ ^1/_2)$	
system	ref.	ε/meV	r_m/Å	ε/meV	r_m/Å	ε/meV	r_m/Å
I–CO_2	this work	44.5	3.99	17.0	4.15	32.0	4.08
I–Xe	7	30.0	4.30	20.5	4.60		
I–Kr	7	24.0	4.05	16.0	4.32		
Br–Xe	7	28.0	3.80	18.4	4.11		
Cl–Xe	8	35.4	3.23	17.0	4.21	20.0	4.09

al.[35] have proposed simple correlation formulae for ion–neutral interactions which depend only on polarizabilities. The find $\varepsilon = 133$ meV and $r_m = 4.27$ Å for XeI^- and $\varepsilon = 90$ meV and $r_m = 4.17$ Å for KrI^-. It is clear that the binding in I^-CO_2 (211 meV, 3.77 Å) is considerably stronger, presumably due to a combination of the charge–quadrupole interaction and charge transfer from the I^- to the CO_2.

We close the discussion by considering in more detail our assumption of T-shaped equilibrium geometry for $I \cdot CO_2$. For I^-CO_2, it is certainly reasonable to expect the I^- to bind to the C atom. This is the geometry favoured by the charge–quadrupole interaction and it also facilitates charge transfer from the I^- to the LUMO of CO_2 (which is why the CO_2 is slightly bent in the anion[21]). The case of the neutral complex seems, *a priori*, more ambiguous. If the I atom acts as an electron donor, it will be attracted to the C atom, while if it acts as en electron acceptor, it will bind to one of the O atoms, resulting in a linear complex. Thus, for example, $Ar \cdot CO_2$ is T-shaped,[36,37] while $CO_2 \cdot HF$ is linear.[38]

Our experiment shows strong evidence for at least a local minimum at the T-shaped geometry of $I \cdot CO_2$. If this were not the case, we would expect to see an extended progression in the van der Waals bending mode as well as in the stretch, whereas our spectra show only a single van der Waals progression. While one could argue that this progression is due entirely to the van der Waals bend and not the stretch, the preceding discussion has shown very strong analogies between the potential-energy curves needed to reproduce our spectra and those which describe the Rg–X interaction. It therefore seems unreasonable to attribute the low-frequency progressions to anything other than the van der Waals stretch. However, we cannot rule out the existence of another minimum at the linear $I \cdot CO_2$ geometry.

Conclusions

We have shown that threshold photodetachment spectroscopy of an anion cluster can provide a detailed probe of weakly bound neutral van der Waals complexes involving open-shell atoms. Specifically, the threshold photodetachment spectrum of I^-CO_2 probes all three electronic states resulting from the electronically anisotropic interaction of $I(^2P_{3/2,\,1/2})$ with a CO_2 molecule. For each electronic state, we observe extensive progressions in the low-frequency C—I van der Waals stretching mode, and we also probe the continuum above the $I + CO_2$ dissociation threshold for two of the three electronic states. From this information, we are able to construct potential-energy curves for the anion and the three neutral electronic states.

Now that we have demonstrated the feasibility of applying this method to a polyatomic open-shell van der Waals complex, we plan to look at some of the diatomic Rg–X species *via* photodetachment of RgX^-. Such experiments would provide a stringent test of the potential-energy functions for these species derived from scattering experiments.

This research is supported by the Air Force Office of Scientific Research under Grant No. AFOSR-91-0084.

Note added in proof

The photoinitiated charge-transfer experiments by Maier and co-workers on $N_2O^+ \cdot Ar$ should have been mentioned in the Introduction.

References

1 J. Goodman and L. E. Brus, *J. Chem. Phys.*, 1977, **67**, 4858.
2 M. T. Berry, M. R. Burstein and M. I. Lester, *Chem. Phys. Lett.*, 1988, **153**, 17; *J. Chem. Phys.*, 1989, **90**, 5878.
3 W. M. Fawzy and M. C. Heaven, *J. Chem. Phys.*, 1988, **89**, 7030; B-C. Chang, L. Yu, D. Cullin, B. Rehfuss, J. Williamson, T. A. Miller, W. Fawzy, X. Zheng, S. Fei and M. Heaven, *J. Chem. Phys.*, 1991, **95**, 7086.
4 P. D. A. Mills, C. M. Western and B. J. Howard, *J. Phys. Chem.*, 1986, **90**, 4961.
5 H. Haberland, *Z. Phys. A*, 1982, **307**, 35.
6 V. Aquilanti and G. Grossi, *J. Chem. Phys.*, 1980, **73**, 1165; V. Aquilanti, G. Liuti, F. Pirani and F. Vecchiocattivi, *J. Chem. Soc., Faraday Trans. 2*, 1989, **85**, 955.
7 C. H. Becker, P. Casavecchia and Y. T. Lee, *J. Chem. Phys.*, 1978, **69**, 2377; 1979, **70**, 2986; C. H. Becker, J. J. Valentini, P. Casavecchia, S. J. Sibener and Y. T. Lee, *Chem. Phys. Lett.*, 1979, **61**, 1; P. Casavecchia, G. He, R. K. Sparks and Y. T. Lee, *J. Chem. Phys.*, 1981, **75**, 710; P. Casavecchia, G. He, R. Sparks and Y. T. Lee, *J. Chem. Phys.*, 1982, **77**, 1878.
8 V. Aquilanti, R. Condori and F. Pirani, *J. Chem. Phys.*, 1988, **89**, 6157; V. Aquilanti, R. Condori, D. Cappelletti, V. Lorent and F. Pirani, *Chem. Phys.*, 1990, **145**, 293; V. Aquilanti, D. Cappelletti, V. Lorent, E. Luzzatti and F. Pirani, *Chem. Phys. Lett.*, 1992, **192**, 153.
9 A. L. Smith and P. C. Kobrinsky, *J. Mol. Spectrosc.*, 1978, **69**, 1.
10 J. J. Ewing and C. A. Brau, *Phys. Rev. A*, 1975, **12**; 129; C. A. Brau and J. J. Ewing, *J. Chem. Phys.*, 1975, **63**, 4640; J. J. Ewing and C. A. Brau, *Appl. Phys. Lett.*, 1975, **27**, 350; C. A. Brau and J. J. Ewing, *Appl. Phys. Lett.*, 1975, **27**, 435.
11 M. F. Golde and B. Thrush, *J. Chem. Phys.*, 1974, **29**, 486.
12 J. Tellinghuisen, J. M. Hoffman, G. C. Tisone and A. K. Hays, *J. Chem. Phys.*, 1976, **64**, 2484; J. Tellinghuisen, G. C. Tisone, J. M. Hoffman and A. K. Hays, *J. Chem. Phys.*, 1976, **64**, 4796; J. Tellinghuisen, A. K. Hays, J. M. Hoffman and G. C. Tisone, *J. Chem. Phys.*, 1976, **65**, 4473; P. C. Tellinghuisen, J. Tellinghuisen, J. A. Coxon, J. E. Velazco and D. W. Sester, *J. Chem. Phys.*, 1978, **68**, 5187; A. Sur, A. Hui and J. Tellinghuisen, *J. Mol. Spectrosc.*, 1979, **74**, 465.
13 M. P. Casassa, M. F. Golde and A. Kvaran, *Chem. Phys. Lett.*, 1978, **59**, 51.
14 I. Dabrowski and G. Herzberg, *J. Mol. Spectrosc.*, 1978, **73**, 183; I. Dabrowski, G. Herzberg and K. Yoshino, *J. Mol. Spectrosc.*, 1981, **89** 491.
15 Y. Tanaka, K. Yoshino and D. E. Freeman, *J. Chem. Phys.*, 1975, **62**, 4484.
16 K. P. Huber and R. H. Lipson, *J. Mol. Spectrosc.*, 1986, **119**, 433.
17 A. Carrington and T. P. Softley, *Chem. Phys.*, 1985, **92**, 199.
18 C. Y. Ng, P. W. Tiedemann, B. H. Mahan and Y. T. Lee, *J. Chem. Phys.*, 1977, **66**, 5737.
19 P. M. Dehmer and J. L. Dehmer, *J. Chem. Phys.*, 1978, **68**, 3462; S. T. Pratt and P. M. Dehmer, *J. Chem. Phys.*, 1982, **76**, 3433.
20 K. Norwood, G. Luo and C. Y. Ng, *J. Chem. Phys.*, 1989, **90**, 4689.

21 D. W. Arnold, S. E. Bradforth, E. H. Kim and D. M. Neumark, *J. Chem. Phys.*, 1992, **97**, 9468.
22 T. N. Kitsopoulos, I. M. Waller, J. G. Loeser and D. M. Neumark, *Chem. Phys. Lett.*, 1989, **159**, 300; C. C. Arnold, Y. Zhao, T. Kitsopoulos and D. M. Neumark, *J. Chem. Phys.*, 1992, **97**, 6121.
23 J. M. Bakker, *J. Phys. E*, 1973, **6**, 785.
24 K. Müller-Dethlefs, M. Sander and E. W. Schlag, *Z. Naturforsch., Teil a*, 1984, **39**, 1089; *Chem. Phys. Lett.*, 1984, **12**, 291; K. Müller-Dethlefs and E. W. Schlag, *Annu. Rev. Phys. Chem.*, 1991, **42**, 109.
25 D. O. Harris, G. G. Engerholm and W. D. Gwinn, *J. Chem. Phys.*, 1965, **43**, 1515.
26 A. S. Dickinson and P. R. Certain, *J. Chem. Phys.*, 1968, **49**, 4209.
27 J. C. Light, I. P. Hamilton and J. V. Lill, *J. Chem. Phys.*, 1985, **82**, 1400.
28 R. B. Metz, Ph.D. Thesis, University of California, Berkeley, 1991.
29 S. E. Bradforth, A. Weaver, D. W. Arnold, R. B. Metz and D. M. Neumark, *J. Chem. Phys.*, 1990, **92**, 7205.
30 G. C. Maitland and E. B. Smith, *Chem. Phys. Lett.*, 1973, **22**, 443.
31 R. J. LeRoy and R. B. Bernstein, *J. Chem. Phys.*, 1970, **52**, 3869.
32 D. Lessen and P. J. Brucat, *J. Chem. Phys.*, 1989, **91**, 4522.
33 C. C. Kirkpatrick and L. A. Viehland, *Chem. Phys.*, 1985, **98**, 221.
34 T. M. Miller, *Handbook of Chemistry and Physics*, CRC Press, Boca Raton, 71st edn., pp. E72–E78.
35 D. Cappelletti, G. Liuti and F. Pirani, *Chem. Phys. Lett.*, 1991, **183**, 297.
36 J. M. Steed, T. A. Dixon and W. Klemperer, *J. Chem. Phys.*, 1979, **70**, 4095.
37 G. T. Fraser, A. S. Pine and R. D. Suenram, *J. Chem. Phys.*, 1988, **88**, 6157.
38 F. A. Baiocchi, T. A. Dixon, C. H. Joyner and W. Klemperer, *J. Chem. Phys.*, 1981, **74**, 6544.
39 E. J. Bieske, A. M. Soliva, A. Friedman and J. P. Maier, *J. Chem. Phys.*, 1992, **96**, 7535.

Paper 2/06257G; *Received* 24*th November*, 1992